






Nested antiferromagnetic spin fluctuations and non-Fermi-liquid behavior in electron-doped $\text{CeCo}_{1-x}\text{Ni}_x\text{In}_5$

H. Sakai ^{*}, Y. Tokunaga , and S. Kambe *Advanced Science Research Center, Japan Atomic Energy Agency, Tokai, Ibaraki 319-1195, Japan*J.-X. Zhu , F. Ronning , and J. D. Thompson *Los Alamos National Laboratory, Los Alamos, New Mexico 87545, USA*H. Kotegawa  and H. Tou *Department of Physics, Kobe University, Kobe 657-8501, Japan*K. Suzuki , Y. Oshima, and M. Yokoyama *Faculty of Science, Ibaraki University, Mito, Ibaraki 310-8512, Japan*

(Received 18 August 2022; revised 26 October 2022; accepted 5 December 2022; published 26 December 2022)

We investigate the electronic state of Ni-substituted $\text{CeCo}_{1-x}\text{Ni}_x\text{In}_5$ by nuclear quadrupole and magnetic resonance (NQR/NMR) techniques. The heavy fermion superconductivity below $T_c = 2.3$ K for $x = 0$ is suppressed by Ni substitutions, and T_c reaches zero for $x = 0.25$. The ^{115}In NQR spectra for $x = 0.125$ and 0.25 can be explained by simulating the electrical field gradient that is calculated for a virtual supercell with density functional theory. The spin-lattice relaxation rate $1/T_1$ indicates that Ni substitution weakens antiferromagnetic correlations that are not localized near the substituent but instead are uniform in space. The temperature (T) dependence of $(T_1T)^{-1}$ for $x = 0.25$ shows a maximum around $T_g = 2$ K and $(T_1T)^{-1}$ decreases toward almost zero when temperature is further reduced as if a gap might be opening in the magnetic excitation spectrum; however, the magnetic specific heat and the static magnetic susceptibility evolve smoothly through T_g with a $-\ln T$ dependence. The peculiar T dependence of $(T_1T)^{-1}$ and non-Fermi-liquid specific heat and susceptibility can be interpreted in a unified way by assuming nested antiferromagnetic spin fluctuations in a quasi-two-dimensional electronic system.

DOI: [10.1103/PhysRevB.106.235152](https://doi.org/10.1103/PhysRevB.106.235152)

I. INTRODUCTION

The heavy fermion superconductor CeCoIn_5 with $T_c = 2.3$ K [1] has been actively studied for more than two decades as new quantum phenomena are continuously discovered. Essential to the intriguing physical properties in CeCoIn_5 , and especially its superconductivity, are the strong spin fluctuations (SFs) that arise from proximity to an antiferromagnetic (AFM) quantum critical point (QCP). Nuclear quadrupole and magnetic resonance (NQR/NMR) measurements have played an important role as a direct probe of the nature of these AFM SFs [2–7]. How close CeCoIn_5 is to an AFM QCP is also demonstrated by many other low-temperature experiments [7–13].

A key question is what is the electronic state that gives rise to these SFs. As a reflection of its proximity to the AFM QCP, slight hole-doping induces long-range AFM order when substituting In $[5s^25p]$ atoms with Cd $[5s^25p^0]$, Hg $[5p^06s^2]$, or Zn $[3d^{10}4s^25p^0]$ in CeCoIn_5 [14,15]. From a microscopic view, Cd or Zn substitutions produce a heterogeneous electronic state where the substituents induce

unscreened localized moments in their immediate vicinity, but the bulk electronic state far from the substituents is unchanged relative to pure CeCoIn_5 [16–18].

In contrast, electron-doping CeCoIn_5 weakens the AFM SFs and provides an opportunity to reveal the underlying electronic state. In the case of Sn $[5s^25p^2]$ substitution for the In sites, AFM SFs are uniformly suppressed as the system is driven away from the AFM QCP [17,19–21] due to a homogeneous strengthening of c - f hybridization [17]. Similarly, Ni $[3d^84s^2]$ substitutions for Co $[3d^74s^2]$ atoms yield a similar superconducting (SC) phase diagram, where T_c is linearly reduced by doping [22]. Interestingly, near the critical electron doping level where $T_c \rightarrow 0$, NFL behavior is observed [22–25], the origin of which is to be determined.

In this paper, we present results of ^{115}In NQR/NMR measurements on Ni-substituted $\text{CeCo}_{1-x}\text{Ni}_x\text{In}_5$. As observed in the Sn-doped system, the AFM fluctuations weaken with Ni substitutions. At the critical composition of $x_c = 0.25$ where T_c approaches zero, an unusual decrease of the NQR/NMR relaxation rate $(1/T_1)$ divided by temperature (T) is observed around ~ 2 K, as if a gap might be opening in the magnetic excitation spectrum. This behavior is distinct from the opening of a real “spin-gap” because NFL behavior continues to

^{*}sakai.hironori@jaea.go.jp

be observed in specific heat, resistivity, and magnetic susceptibility.

In Sec. II, the experimental methods are described. In Sec. III A, ^{115}In NQR spectra of the two crystallographically distinct In(1) and In(2) sites under zero magnetic field are compared with the calculated NQR spectra. In Sec. III B, the frequency dependence of the nuclear spin-lattice relaxation rate $1/T_1$ is shown. Here, spatial homogeneity of the electronic state is revealed and discussed. In Sec. III C, the T dependence of $1/T_1$ is presented. The site-dependent response and NMR T_1 results with an applied field H_0 are also shown. In Sec. IV, we calculate the T dependence of $(T_1 T)^{-1}$ and the logarithmic increase of the magnetic specific heat coefficient C_m/T using a mode-mode coupling theory that considers nesting of AFM SFs in itinerant electronic degrees of freedom.

II. EXPERIMENTAL METHODS

Single crystals of $\text{CeCo}_{1-x}\text{Ni}_x\text{In}_5$ with $x = 0.125, 0.25$, and 0.3 were grown by means of the indium-flux technique [22]. Energy-dispersive x-ray spectroscopy (EDS) confirmed these crystals' chemical homogeneity. Inductively coupled plasma mass spectrometry and EDS identified that the nominal and measured x values were in reasonable agreement, with a maximal deviation of $\Delta x/x \sim 17\%$. For simplicity, this paper uses the nominal x values for Ni-doped samples.

Crystals for NQR/NMR measurements were selected from the identical batches used for magnetic susceptibility, electrical resistivity, and specific-heat measurements [22,25]. For each NQR/NMR experiment, a single crystal with a typical dimension of $3 \times 3 \times 0.2 \text{ mm}^3$ was tightly wound by a thin copper wire with a diameter of $50\text{--}150 \mu\text{m}$ to form a solenoid coil for radio-frequency (rf) excitations. The coil with the sample was mounted on an NQR/NMR probe with two variable capacitors to tune the resonance frequencies and match the rf circuit's impedance. The NQR/NMR experiments were carried out in ^4He and ^3He - ^4He cryostats and performed using a phase-coherent, pulsed spectrometer. External magnetic fields (H_0) were applied using a highly homogeneous NMR-grade SC magnet. To form the nuclear spin echoes, $90^\circ - 180^\circ$ conditions were used with a first pulse duration of $20\text{--}30 \mu\text{sec}$ and with the smallest possible power to avoid rf heating of the sample. The separation τ between the first and second pulses was typically $30\text{--}50 \mu\text{sec}$. Frequency-swept spectra were measured by tuning the rf network at each frequency in steps of $10\text{--}50 \text{ kHz}$.

Using conventional notation, the quadrupole frequency parameter is defined as $\nu_Q \equiv \frac{3e^2qQ}{2I(2I-1)\hbar}$, where eQ is the nuclear quadrupolar moment, I is the nuclear spin quantum number, and $eq \equiv V_{ZZ}$ is the principal component of the electric field gradient (EFG) tensor. The EFG asymmetry parameter is defined as $\eta \equiv \frac{|V_{YY} - V_{XX}|}{|V_{ZZ}|}$.

EFGs were calculated by density functional theory (DFT) [20] assuming 12.5% Ni doping in a $2 \times 2 \times 2$ supercell. The DFT calculations were performed using the WIEN2K code [26] with the exchange-correlation functional of Perdew, Burke, and Ernzerhof under the generalized gradient approximation [27]. Spin-orbit coupling was included via a second-order variational scheme.

The nuclear spin-lattice relaxation time T_1 was measured using the inversion-recovery method with a π pulse. To evaluate NQR T_1 for In nuclei, each recovery curve $R(t)$ was fit by the recovery function for the $4\nu_Q$ ($|\pm \frac{9}{2}\rangle \leftrightarrow |\pm \frac{7}{2}\rangle$) transition line of $I = 9/2$ with a single T_1 : $R(t) \propto (4/33)\exp(-3t/T_1) + (80/143)\exp(-10t/T_1) + (49/165)\exp(-21t/T_1) + (16/715)\exp(-36t/T_1)$, which is derived assuming the asymmetry parameter $\eta = 0$. In the case of finite η , the recovery function was calculated by numerically diagonalizing the master equation for nuclear relaxation [28].

III. RESULTS

A. Experimental and simulated ^{115}In NQR spectra in Ni-substituted CeCoIn_5

CeCoIn_5 has a simple layered tetragonal structure, as shown in Fig. 1(a). There are two crystallographically inequivalent In sites denoted as In(1) ($4/mmm$) and In(2) ($2mm$). As shown in Fig. 1(b), T_c decreases as Ni concentrations x increase in $\text{CeCo}_{1-x}\text{Ni}_x\text{In}_5$, and it becomes zero at $x = 0.25$. The NQR spectra for the $4\nu_Q$ transition of In(1) and the $3\nu_Q$ transition of In(2) of 12.5% Ni-doped CeCoIn_5 are simulated using a $2 \times 2 \times 2$ supercell as presented in Fig. 1(c). The NQR lines were calculated using the same procedure used previously [17,18]. Figures 1(d) and 1(e) show the experimental results in the paramagnetic state of nondoped, 3% Sn (actual) [17]-, 12.5% Ni-, and 25% Ni-doped CeCoIn_5 .

In the Sn-doped case [17], line splitting is somewhat complicated because the substituents are distributed across both In(1) and In(2) sites. As shown in Fig. 1(d), the local EFGs for four peaks labeled A, B, C, and D can be resolved. The B and C peaks can be assigned to the first nearest neighboring (NN) In(1) sites from the Sn dopants on the In(1) and In(2) sites, respectively. As for the In(2) sites shown in Fig. 1(e), the line is broadened, which may be due to a less-discrete distribution of EFGs induced on the In(2) sites by substitution.

In the 12.5% and 25% Ni-doped cases, the In(1) NQR line remains as a single peak, as seen in Fig. 1(e), although the linewidth broadens slightly. The In(1) site is far from the Ni substituent. In contrast, the In(2) line for the case of 12.5% Ni doping has a subpeak B that emerges on the low-frequency side of the main peak A, as shown in Fig. 1(e).

To simulate the 12.5% Ni-doped case, as shown in Fig. 1(c), we assume a $2 \times 2 \times 2$ superlattice of CeCoIn_5 in which Ni dopants replace Co atoms in the eight corners. In the $2 \times 2 \times 2$ superlattice, In(1) sites locate in an identical environment, i.e., every In(1) site is situated in the center of the square of Ce atoms where one-eighth of the nearest Co is replaced by a Ni dopant. The four In(2) sites have different local environments and are labeled as In(2)-1, -2, -3, and -4. Here the label's number corresponds to the distance from the Ni dopant, i.e., In(2)-1 is closest and In(2)-4 is farthest from the Ni dopant. The calculated results are summarized in Table I. The EFG is calculated for every In site, and then they are summed. To compare with experimental results, the computed spectral frequencies are multiplied by a factor of ~ 0.9 , which may be attributed to screening of EFGs by

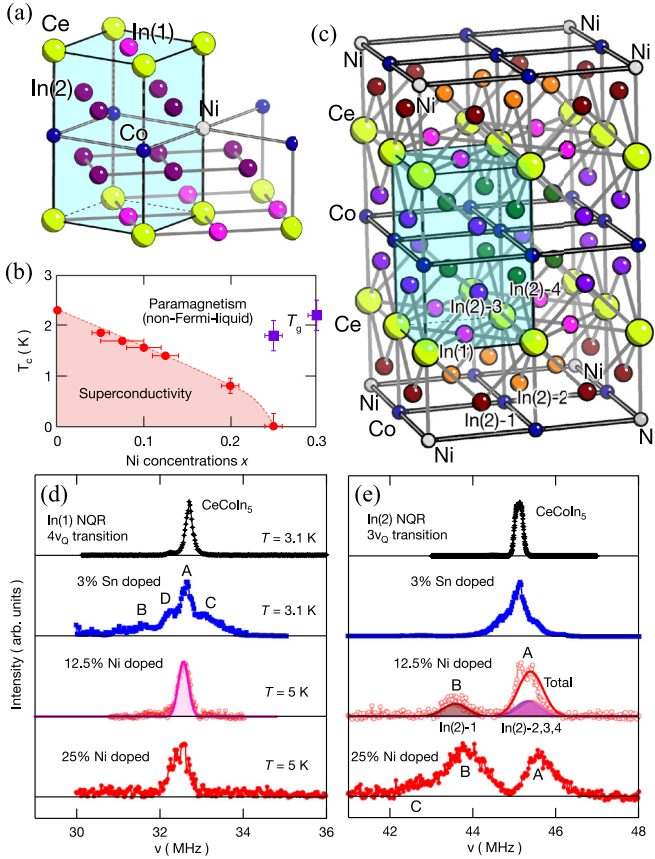


FIG. 1. (a) Crystal structure of CeCoIn₅ and Ni substitution site. (b) T - x phase diagram of CeCo_{1-x}Ni_xIn₅ obtained from temperature variations of ac susceptibility, magnetization, electrical resistivity, and specific heat [22]. The characteristic temperature T_g is also plotted, defined as the temperature at which the broad maximum of $(T_1 T)^{-1}$ appears (see text in Sec. III C). The dotted line is a guide to the eyes. (c) The assumed 222 supercell for 12.5% Ni doping. (d) In(1)- $4\nu_Q$ and (e) In(2)- $3\nu_Q$ NQR spectra for CeCoIn₅, 3% Sn-doped [17], 12.5% Ni, and 25% Ni-doped CeCoIn₅ in the paramagnetic (normal) state. The calculated NQR spectra for 12.5% Ni doped CeCoIn₅ are also plotted as the solid curve. The labels A, B, C, and D indicate the respective spectral positions.

conduction electrons in the real lattice. A similar approach has been reported earlier [29].

From the DFT calculation of ν_Q shown in Fig. 1(e), the subpeak B can be assigned to In(2)-1 sites in Fig. 1(c), i.e., the first NN In(2) sites from the Ni substituent. The NQR lines for the other In(2)-2, -3, and -4 sites appear at approximately the same position A, so the A peak intensity is larger than that at the B peak. Another subpeak, C, appears for $x = 0.25$ and is assigned to In(2) sites with two NN Ni substituents.

B. Spin-lattice relaxation rates $1/T_1$ proving homogeneous electronic states

To examine the homogeneity of the electronic state, the frequency dependence of the nuclear-spin relaxation rate $1/T_1$ was measured as shown in Fig. 2. The nuclear magnetization recovery at each frequency was taken using the weak rf-pulse condition to excite a narrow-frequency window. Generally,

TABLE I. The simulated nuclear quadrupolar frequency ν_Q and the asymmetric parameter η of the EFG for In(1) sites and In(2)-1, -2, -3, and -4 sites in the superlattice shown in Fig. 1(c).

In	Sites	ν_Q (MHz)	η
In(1) ^a	—	9.354 47	0.031 84
In(2) ^b	1	16.12	0.2702
	2	16.6756	0.2702
	3	16.6535	0.2728
	4	16.6906	0.263 86

^aThe ν_Q value is multiplied by a factor of 0.87 as explained in the text.

^bThe multiplicative factor of ν_Q is 0.927.

$1/T_1$ in units of $k_B = \hbar = 1$ can be expressed [30] as

$$\frac{1}{T_1} = 2T\gamma_n^2 \sum_{\mathbf{q}} A_{\perp}^2(\mathbf{q}) \frac{\text{Im}\chi_{\perp}(\mathbf{q}, \omega_0)}{\omega_0}, \quad (1)$$

where $A(\mathbf{q})$ is the \mathbf{q} -dependent hyperfine coupling constant, $\text{Im}\chi(\mathbf{q}, \omega_0)$ is the imaginary part of the dynamical susceptibility, ω_0 is the nuclear Larmor frequency, and \perp refers to the component perpendicular to the quantization axis. From Eq. (1), $1/T_1$ divided by temperature, i.e., $(T_1 T)^{-1}$, is proportional to the \mathbf{q} summation of dynamical magnetic susceptibility. Therefore, the frequency dependence of $1/T_1$ shown in Fig. 2 tells us the local distribution of SFs.

The local circumstance for In(1) sites introduced by the Ni dopants is not distributed much since the peak remains a single peak, which is also expected from the above NQR simulation. As shown in Fig. 2(a), for the $4\nu_Q$ peak, the variation of $1/T_1$ for In(1) sites at 5 K is within 15% at most in the full-width at the half maximum (FWHM). In the case of In(2), multiple peaks are expected due to the difference in local circumstances as explained in the NQR simulation. For the In(2) sites, the average $1/T_1$ values within the FWHM at the respective A, B, and C peaks are the same within 15%, as shown in Fig. 2(b). Thus, the site-to-site distribution of $1/T_1$ within each spectral peak of In(1) and In(2) is relatively small. Namely, a homogeneous electronic state is realized in

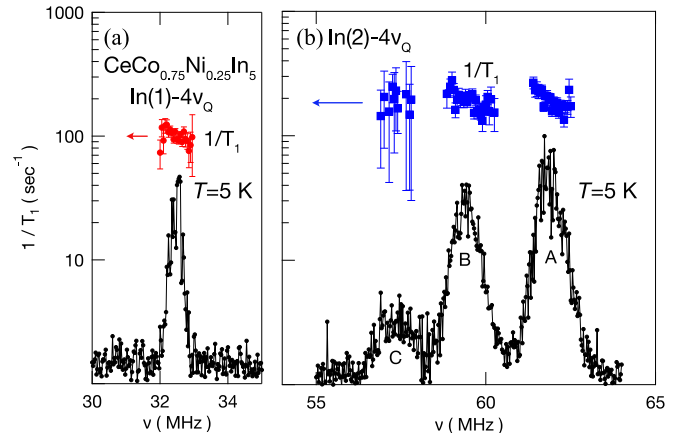


FIG. 2. Frequency dependence of $1/T_1$ for $4\nu_Q$ transitions of (a) In(1) and (b) In(2) sites in 25% Ni-doped CeCoIn₅, respectively. The NQR spectra are overlaid.

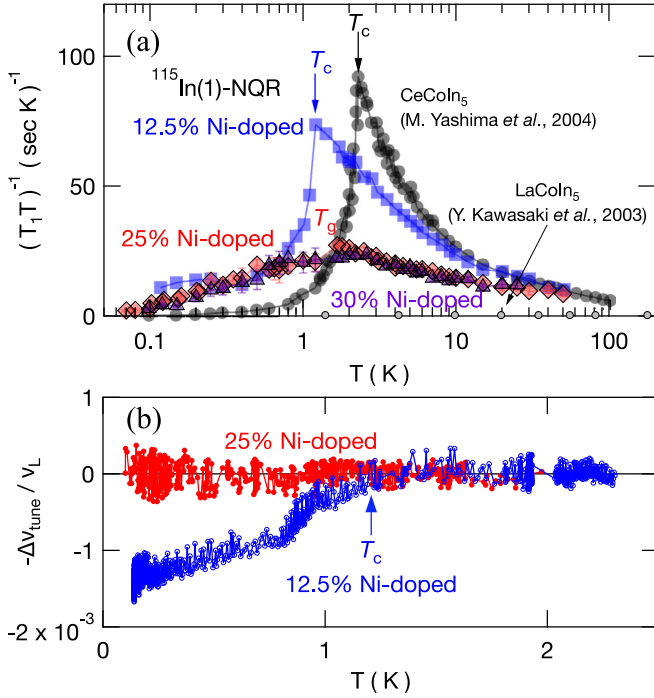


FIG. 3. (a) Temperature dependence of $(T_1 T)^{-1}$ for In(1) NQR in 12.5%, 25%, and 30% Ni-doped CeCoIn₅. The data for LaCoIn₅ [4] and CeCoIn₅ [5] are also shown. The solid lines simply connect adjacent data points for each set. (b) Temperature dependence of $-\Delta\nu_{\text{tune}}/\nu_L$ for 12.5% and 25% Ni-doped CeCoIn₅ with $\nu_L = 32.7$ MHz.

the Ni-doped case, as in the case of Sn doping [17]. This is in contrast to the heterogeneous electronic state in CeCoIn₅ hole-doped by Cd [17] or Zn [18]. For these hole-doped systems, $1/T_1$ values of the main peak and the subpeak are quite different; e.g., for the 1.5% Cd-doped case at 5 K, the subpeak $1/T_1 = 460 \text{ sec}^{-1}$ is about twice as large as the main peak $1/T_1 = 240 \text{ sec}^{-1}$.

C. Temperature dependence of spin-lattice relaxation rates $1/T_1$

Figure 3(a) shows the T dependence of $(T_1 T)^{-1}$ for In(1) NQR in nondoped and 12.5%, 25%, and 30% Ni-doped CeCoIn₅. In CeCoIn₅, $(T_1 T)^{-1}$ increases significantly on cooling below 100 K due to the presence of AFM SFs in the normal state and then sharply decreases at T_c as the superconducting gap develops. While the abrupt disappearance of a signature for AFM SFs below T_c suggests magnetically mediated SC pairing, we do not know what kind of electronic state would appear if superconductivity had not occurred.

With 12.5% Ni doping, $(T_1 T)^{-1}$ in the normal state decreases slightly from that for nondoped CeCoIn₅. In addition to a sudden decrease of $(T_1 T)^{-1}$, a change of the resonant frequency is also observed at $T_c = 1.2$ K, as shown in Fig. 3(b). The resonant frequency of the LC circuit is $\nu_{\text{tune}} = (2\pi\sqrt{LC})^{-1}$, where L and C are the inductance and capacitance, respectively. If the ac susceptibility (χ') is reduced due to SC diamagnetism, $L = L_0(1 + \epsilon\chi')$ should decrease (ϵ is the filling factor of the sample in the coil). Consequently, the onset T_c is detected *in situ* by tracking $-\Delta\nu_{\text{tune}}/\nu_L$. In this

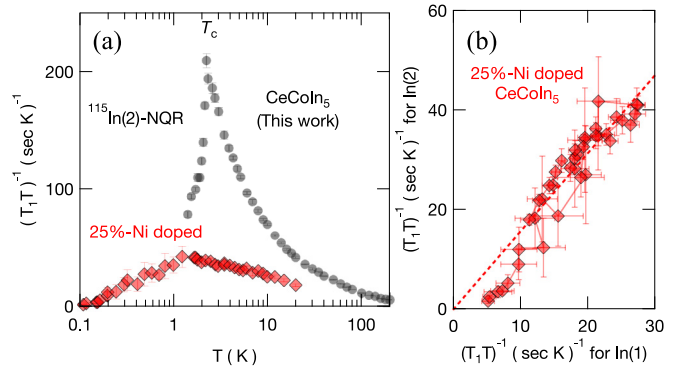


FIG. 4. (a) Temperature dependence of $(T_1 T)^{-1}$ for In(2) NQR in nondoped and 25% Ni-doped CeCoIn₅. (b) The plot of $(T_1 T)^{-1}$ for In(2) NQR vs $(T_1 T)^{-1}$ for In(1) NQR using temperature as an implicit parameter in 25% Ni-doped CeCoIn₅.

experiment, we set $\nu_L = 32.7$ MHz by tuning the variable capacitors, which were fixed during the subsequent measurements. $\Delta\nu_{\text{tune}}$, then, reflects the change in inductance due to the onset of superconductivity.

For 25% Ni-doped CeCoIn₅, evidence for superconductivity is not observed above our base temperature of ~ 0.1 K, as seen in Fig. 3(b). This is consistent with the T - x phase diagram of $\text{CeCo}_{1-x}\text{Ni}_x\text{In}_5$ [Fig. 1(b)] reported earlier [22]. Figure 3(a) shows that $(T_1 T)^{-1}$ in the normal state above $T_g \sim 2$ K is reduced considerably relative to the relaxation rate for nondoped and 12.5% Ni-doped CeCoIn₅. Though reduced, these $(T_1 T)^{-1}$ values are still substantially enhanced relative to those in the non-4*f* material LaCoIn₅ [4] and signal the continued presence of SFs.

Even though superconductivity is absent, $(T_1 T)^{-1}$ decreases below T_g , as if a gap might be opening in the magnetic excitation spectrum. To confirm that such an unusual decrease of $(T_1 T)^{-1}$ is intrinsic, we measured $1/T_1$ using a different single crystal and found that the results were unchanged. Specific heat measurements were also performed using these crystals, with results identical to those reported [22]. Increasing the Ni concentration to 30% does not significantly change $(T_1 T)^{-1}$ values over the whole temperature range as shown in Fig. 3(a).

To see the site dependence, we measured the In(2) NQR relaxation rate. Since the principal axis of the EFG is different between In(1) and In(2) sites, which are along the c and a axes, respectively, this gives information on the anisotropy of $\text{Im}\chi(\mathbf{q}, \omega_0)$. As shown in Fig. 4(a), the temperature dependence of $(T_1 T)^{-1}$ for In(2) sites in 25% Ni-doped CeCoIn₅ is similar to that for In(1) as shown in Fig. 3(a). Namely, an unusual decrease of $(T_1 T)^{-1}$ is observed as in In(1) NQR. Thus, the decrease of $(T_1 T)^{-1}$ at T_g is independent of the hyperfine form factor.

A linear relationship between $(T_1 T)^{-1}$ at In(2) and In(1) sites, shown in Fig. 4(b), has a slope $\rho(T_1^{-1})$ of about 1.56 ± 0.03 . For comparison, $\rho(T_1^{-1})$ is 2.53 ± 0.05 in the normal state of CeCoIn₅. If we define the rate $R_i \equiv \sum_{\mathbf{q}} \text{Im}\chi_i(\mathbf{q}, \omega_0)/\omega_0$ ($i = a$ and c), then from Eq. (1) $(1/T_1 T)_{\text{In(1)}} = 2A_a^2(1)R_a$ and $(1/T_1 T)_{\text{In(2)}} = A_a^2(2)R_a + A_c^2(2)R_c$, where $A_i(n)$ is the hyperfine coupling constant for the In(n) sites. As discussed above, the

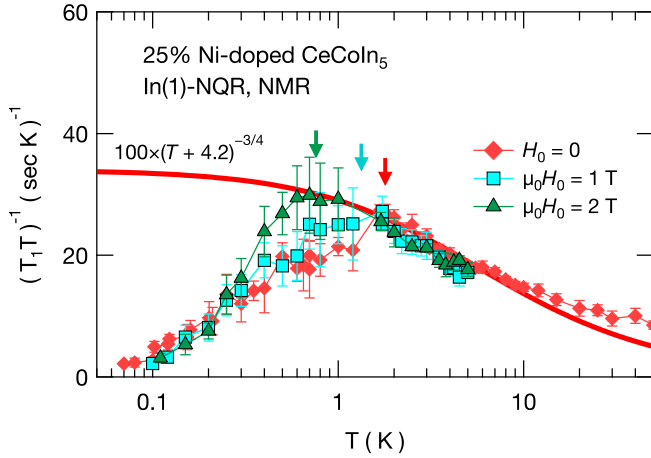


FIG. 5. Temperature dependence of $(T_1T)^{-1}$ for the In(1) sites with applying magnetic fields of $\mu_0H_0 = 1$ and 2 T. The corresponding NQR $(T_1T)^{-1}$ is included for comparison. The thick curve represents a fit to the anisotropic AFM SF model (see text).

hyperfine form factor plays no significant role, and consequently we assume $f^2(\mathbf{q}) = 1$, which implies $A^2(\mathbf{q}) = A_i^2(n)f^2(\mathbf{q})$ in Eq. (1). Taking a Lorentzian form for $\text{Im}\chi_i(\mathbf{q}, \omega_0)$ with magnetic fluctuation energy $\Gamma(\mathbf{q})$, $\text{Im}\chi_i(\mathbf{q}, \omega_0)/\omega_0 = \chi_i(\mathbf{q})/\Gamma_i(\mathbf{q})$. Within the strongly correlated limit approximation $2\pi\chi_i(\mathbf{q})\Gamma_i(\mathbf{q}) \sim 1$ [31], so the q -averaged (local) magnetic fluctuation energy $\langle\Gamma_i\rangle \equiv [\Gamma_i(\mathbf{q}^2)]^{1/2}$, and thus $R_i = 1/(2\pi(\Gamma_i)^2)$.

Using $A_i(n)$ obtained previously [2,32], $\rho(T_1^{-1}) = 2.53$ for CeCoIn_5 leads to $\langle\Gamma_c\rangle/\langle\Gamma_a\rangle = 1.28$. Similarly, $\rho(T_1^{-1}) = 1.56$ for the Ni-doped case leads to $\langle\Gamma_c\rangle/\langle\Gamma_a\rangle = 1.72$, assuming the same $A_i(n)$. The fact that $\langle\Gamma_c\rangle/\langle\Gamma_a\rangle > 1$ for both compounds indicates XY -type anisotropy of the AFM SFs. XY -type AFM SFs are also deduced from ^{59}Co NMR experiments on CeCoIn_5 [6]. The primary conclusion from this analysis is that the anisotropy of AFM SFs does not change significantly with Ni doping.

The AFM anisotropy appears to differ from that of the uniform magnetic susceptibility [1,25]. This may be related to the fact that magnetic correlations or spin polarization depends on the wave vector \mathbf{q} . Indeed, XY -type correlations in neutron scattering are found at a commensurate AFM \mathbf{Q}_0 [33,34], while a spin-resonance excitation that develops below T_c in CeCoIn_5 occurs at a commensurate [33,35] (or weakly incommensurate [36]) AFM \mathbf{Q}_0 (or \mathbf{Q}^*) and is polarized along the c axis [33,35,36]. In contrast, the polarization of the AFM moments changes from the c axis to nearly the c plane when there is a commensurate-incommensurate AFM transition in Zn-doped CeCoIn_5 [18].

Figure 5 shows the temperature dependence of $(T_1T)^{-1}$ for In(1) NQR and NMR measured at $\mu_0H_0 = 1$ and 2 T. For CeCoIn_5 , $1/T_1$ is known to vary approximately as $T^{1/4}$ in the normal state [2], which is explained by the anisotropic AFM SF model when a system is in proximity to an AFM QCP [4]. In this model, $(T_1T)^{-1}$ is proportional to the staggered susceptibility $\chi(\mathbf{Q})^{-3/4} \propto (T + \theta)^{-3/4}$ for a certain AFM $\mathbf{q} = \mathbf{Q}$ vector [37] and θ is a measure of how close the system is to the AFM QCP. Using this model to fit the NQR data for

$T_g < T < 10$ K in 25% Ni-doped CeCoIn_5 gives $\theta = 4.2$ K, as shown in Fig. 5. Since $\theta = 0.6$ K for CeCoIn_5 [4], the larger θ value indicates that the Ni-doping moves the system away from an AFM QCP, but its still relatively small value implies that SFs still should be present at 25% Ni doping.

When applying a magnetic field, the normal state $(T_1T)^{-1}$ does not change significantly. $(T_1T)^{-1}$ continues to show an unusual decrease below $T_g(H_0)$, even under $\mu_0H_0 = 1$ and 2 T. As indicated by the down arrows in Fig. 5, T_g shifts to lower temperature with increasing applied field, although the Knight shift does not change at $T_g(H_0)$. $(T_1T)^{-1}(H_0)$ above $T_g(H_0)$ follows the same curve that is a fit to the anisotropic AFM SF model for $H_0 = 0$.

One may consider that preformed SC pairs may cause the unusual decrease in $(T_1T)^{-1}$ below T_g . If Cooper pairs were preformed around $T_g(H_0 = 0)$, an externally applied field should suppress the pair preformation, $T_g(H_0 > 0)$ should decrease relative to $T_g(H_0 = 0)$, and $(T_1T)^{-1}$ at $T_g(H_0 = 0)$ should increase. In this SC fluctuation scenario, however, the Knight shift and magnetic susceptibility also should decrease below T_g , as observed in the slightly over-doped high- T_c cuprate $\text{TiSr}_2\text{CaCu}_2\text{O}_{6.8}$ [38,39]. We, however, do not observe such a decrease in Knight shift and magnetic susceptibility, so we consider this scenario unlikely.

IV. DISCUSSIONS

A framework is needed to explain the decrease in $(T_1T)^{-1}$ below T_g without opening an energy gap in the spin-excitation spectrum to be consistent with the NFL behavior of the specific heat and magnetic susceptibility that is present through a temperature range encompassing T_g . (Figure 6(b) gives an example of NFL behavior of the magnetic specific heat divided by temperature for 25% Ni-doped CeCoIn_5 [22].)

A key to understanding this apparently paradoxical behavior would be the strongly q -dependent AFM SFs in CeCoIn_5 [4,5,7,33,34,36,41] and its doped alloys [16–18,42]. In general, $(T_1T)^{-1}$ reflects these AFM SFs because it is composed of the spectral weight of SFs integrated over a wide q range. The suppression of spectral weight of SFs with a specific AFM mode in this situation should yield a reduction of $(T_1T)^{-1}$ while not significantly changing the specific heat and uniform magnetic susceptibility.

Here, we consider the idea of nested AFM SFs based on an itinerant-localized duality picture [43] that was introduced originally by Miyake and Nariakiyo [44]. It is a modification of the self-consistent renormalization (SCR) theory by Moriya *et al.* [31,45,46], which treats mode-mode couplings of spatially extended spin-density fluctuations in a self-consistent fashion.

The dynamical susceptibility near an AFM instability at the wave vector $\mathbf{q} = \mathbf{Q}$ can be expanded for small \mathbf{q} and small ω as

$$\frac{1}{\chi(\mathbf{Q} + \mathbf{q}, \omega)} = \frac{1}{\chi(\mathbf{Q})} + Aq^2 - iC\omega, \quad (2)$$

where A and C are finite coefficients reflecting the electronic band structure. In the original SCR model, the dynamical susceptibility is characterized by two energy scales, $T_0 \equiv \Gamma_q^2/(2\pi)$ ($\Gamma = A/C$) and $T_A \equiv Aq_B^2/2$, that correspond to the

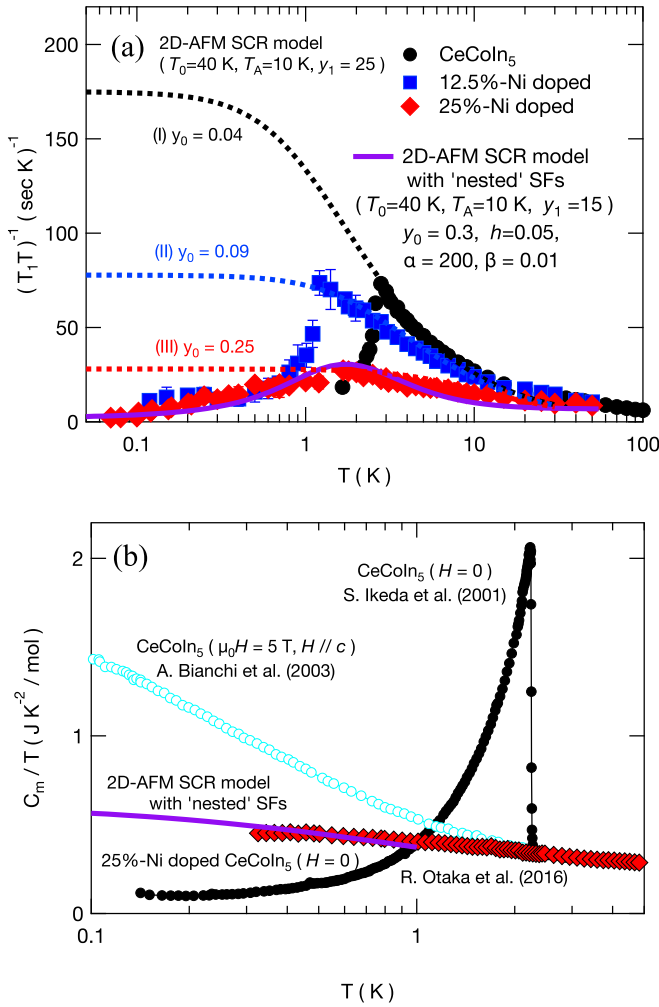


FIG. 6. (a) The solid curve is a calculation of $(T_1T)^{-1}$ for 25% Ni-doped CeCoIn₅ by the modified two-dimensional (2D)-AFM SCR model assuming nested AFM SFs. The dashed curves also show calculations using the 2D-AFM SCR model without nested SFs. (b) Experimental data [22] and calculation of the electronic specific heat divided by temperature, called the Sommerfeld coefficient in the text, for 25% Ni-doped CeCoIn₅ using the same parameters applicable to a description of $(T_1T)^{-1}$ within the context of the modified 2D-AFM SCR model with nesting. The specific heat for CeCoIn₅ under $H_0 = 0$ [40] and $\mu_0H_0 = 5$ T along the c axis [9] is also plotted for comparison.

SF energy in ω and q spaces, respectively. The q dependence of an effective RKKY interaction J_Q is expressed as $J_Q - J_{Q+q} = 2T_A(|q|/|q_B|)^2$ around the AFM wave vector Q , where q_B is the zone-boundary vector. Defining the dimensionless inverse static susceptibility $y = [2T_A\chi(Q)]^{-1}$ allows the dynamical susceptibility in the case of 2D AFM to be written as $[2T_A\chi(Q+q, \omega)]^{-1} = y + (q/q_B)^2 - i\omega/(2\pi T_0)$. The self-consistent equation for y is given using two more parameters, $y_0 \equiv [2T_A\chi(Q, 0)]^{-1}$ and $y_1 \equiv 2J_Q/(\pi^2 T_A)$, by

$$y = y_0 + y_1 \int_0^{x_c} x \left[\ln u - \frac{1}{2u} - \psi(u) \right] dx, \quad (3)$$

with $u = (y + x^2)/t$ and $t = T/T_0$, where $\psi(u)$ is the digamma function and x_c is the reduced cutoff wave vector

of order unity. Here, y_0 is a measure of proximity to the QCP, $y_0 = 0$ defining the QCP, and y_1 reflects the strength of dispersion of the effective RKKY exchange interaction J_Q .

The SCR theory has been applied successfully to characterize the nature of SFs in many heavy-fermion materials [47,48]. Indeed, $(T_1T)^{-1} \propto (2\pi T_A T_0 y)^{-1}$ from the 2D-AFM SCR model reproduces experimental results of $(T_1T)^{-1}$ for CeCoIn₅ [7] and, as shown in Fig. 6(a), the normal state relaxation rate of 12.5% and 25% Ni-doped CeCoIn₅. For 12.5% Ni doping, only a somewhat larger $y_0 = 0.09$ than the $y_0 = 0.04$ for CeCoIn₅ can explain its reduced $(T_1T)^{-1}$ without changing other parameters (T_0 , T_A , y_1). However, the model cannot explain the decrease in $(T_1T)^{-1}$ below T_g in the 25% Ni-doped sample.

Following Miyake and Narikiyo [49], we introduce a new parameter h that is a measure of the deviation of Fermi surfaces from perfect nesting ($h = 0$). Now the SCR formula in Eq. (3) in the itinerant regime becomes

$$y = y_0 \frac{\tau^2}{1 + \alpha \tau^2} + y_1 \frac{\tau^2}{(1 + \alpha \tau^2)^2} \times \int_0^{x_c} x \left[\ln u - \frac{1}{2u} - \psi(u) \right] dx, \quad (4)$$

with $u = \beta(1 + \alpha \tau^2)(y + x^2)/(\tau t)$ and $\tau \equiv \sqrt{t^2 + h^2}$. Here, α and β are the dimensionless representation of renormalized A and C parameters, respectively. That is, the coefficients α and β depend on the band structure modified by h . In contrast to the original SCR model, A and C are allowed to be strongly T dependent.

In this extended SCR model, the nuclear-spin relaxation rate can be deduced [44] as

$$(T_1T)^{-1} \propto \frac{C}{A^2} \left(\frac{1}{y} - \frac{1}{y+1} \right). \quad (5)$$

If nesting is satisfied ($h \ll 1$) and assuming a 2D circular band structure, $A = 7\zeta(3)v_F^2/(32\pi^2 T^2)$ and $C = \pi/(8T)$, where $\zeta(3)$ and v_F are the Apéry's constant and the renormalized Fermi velocity, respectively. In this limit, $\chi(Q)$ increases as T decreases, but the ratio C/A^2 decreases as T^{-3} . For some sets of parameters, then, a “spin-gap”-like behavior will appear in the low- T region without opening a gap in the SF spectrum.

If we slightly increase y_0 to be 0.3 from its value $y_0 = 0.04$ for CeCoIn₅ and assume a small departure from perfect nesting, $h = 0.05$, $(T_1T)^{-1}$ that is calculated from Eq. (5) reproduces the unusual decrease below T_g as shown in Fig. 6(a). For example, if a larger $h \sim 0.3$ were assumed, the unusual decrease disappears, as shown in Ref. [44]. Also, if y_0 is set closer to zero with $h = 0.05$, $(T_1T)^{-1}$ diverges, and the unusual decrease becomes invisible. In other words, in non-doped CeCoIn₅, due to $y_0 \sim 0$, the nesting character of AFM SFs cannot be observed. It is necessary for the system to be tuned slightly away from the AFM-QCP to reveal the unusual decrease of $(T_1T)^{-1}$. Simultaneously, another necessary condition is minimal h : Fermi surfaces should have a nesting character.

To confirm the validity of these modified SCR parameters, the T dependence of the Sommerfeld coefficient γ in specific heat was calculated using the same parameters obtained above. At the lowest temperatures, γ_{coh} , which is the

Sommerfeld coefficient that is enhanced by interactions relative to γ_0 in the absence of interactions, is given [44] as

$$\gamma_{\text{coh}} \propto \left[\frac{3\pi}{4}h + \frac{2\pi^2}{3}h \ln \frac{1+\eta}{\eta} \right], \quad (6)$$

with $\eta = 2T_A\gamma$. With parameters that account for $(T_1T)^{-1}$ in 25% Ni-doped CeCoIn₅, we use Eq. (6) to calculate γ_{coh} that is compared to experimental results in Fig. 6(b). The calculations account well for experimental observations, including the absence of any anomaly at T_g . In this material, the logarithmic divergence of γ at low temperatures [22,25] is much weaker than in CeCoIn₅ subjected to a field $\mu_0H_0 = 5$ T along the c axis [9], indicating that γ_0 becomes slightly larger by Ni doping. Similar calculations apply to the uniform susceptibility that also exhibits NFL behavior in 25% Ni-doped CeCoIn₅ [22,25].

Thus, the unexpected decrease of $(T_1T)^{-1}$ below T_g and the NFL behavior observed in specific heat, resistivity, and magnetic susceptibility can be understood in the framework of the 2D-AFM SCR model with nested AFM SFs that cause a decrease of integrated spectral weight of coherent SFs.

V. CONCLUSION

Because the Ni substituents occupy sites between Ce-In blocks, this substitution allows the $4f$ electronic state to be investigated cleanly. We have observed a gradual decrease of AFM SFs by Ni substitutions for In that both electron-dope and shift CeCoIn₅ away from an AFM-QCP. An important finding is that $(T_1T)^{-1}$ exhibits an unusual decrease below T_g at the critical 25% Ni-doping level, although NFL behavior persists in other properties. By introducing the concept of nested AFM SFs, these seemingly contradictory experimental facts can be understood in a unified manner. The nested AFM SFs result from the quasi-2D nature of the original band structure in CeCoIn₅, which is

experimentally established by de Haas–van Alphen oscillations [50,51] and angle-resolved photoemission spectroscopy studies [52,53].

Since the 2D-AFM SCR model with nested AFM SFs is still phenomenological, further investigation is required to clarify the relationship between parameters that have been introduced. It would be worthwhile to see if there are other physical quantities besides NQR/NMR $(T_1T)^{-1}$ that exhibit an unusual behavior in Ni-doped CeCoIn₅, e.g., Hall resistance or thermoelectric power enhancements at T_g predicted by the 2D-AFM SCR model with nested AFM SFs. One may also ask what Q is nesting, e.g., a commensurate Q_0 or an incommensurate Q^* ? With our simplified model, however, it is not possible to resolve whether the NFL behavior in Ni-doped CeCoIn₅ arises from fluctuations around Q_0 or Q^* . In the duality picture by Miyake and Narikiyo [44], the wave vector Q of the itinerant part tends to be incommensurate. In contrast, that of the local spin part is commensurate. For further microscopic understanding, inelastic neutron scattering studies will be helpful.

ACKNOWLEDGMENTS

We are grateful for stimulating discussions with R. Otaka, E. D. Bauer, T. Park, Y. Tokiwa, Y. Haga, and K. Miyake. Work at Los Alamos was performed under the auspices of the U.S. Department of Energy, Office of Science, Division of Materials Science and Engineering. DFT calculations were performed with support from the LANL LDRD program. Computational resources was provided by Center for Integrated Nanotechnologies, a DOE BES user facility, in partnership with the LANL Institutional Computing Program. A part of the NQR work was performed using the ³He-⁴He dilution refrigerator installed in Kobe University through JSPS KAKENHI Grant No. 15H05885 (J-Physics). A part of this work was also supported by JSPS KAKENHI Grants No. JP16KK0106, No. JP17K05522, No. JP17K05529, and No. JP20K03852 and by the JAEA REIMEI Research Program.

- [1] C. Petrovic, P. G. Pagliuso, M. F. Hundley, R. Movshovich, J. L. Sarrao, J. D. Thompson, Z. Fisk, and P. Monthoux, *J. Phys.: Condens. Matter* **13**, L337 (2001).
- [2] Y. Kohori, Y. Yamato, Y. Iwamoto, T. Kohara, E. D. Bauer, M. B. Maple, and J. L. Sarrao, *Phys. Rev. B* **64**, 134526 (2001).
- [3] N. J. Curro, J. L. Sarrao, J. D. Thompson, P. G. Pagliuso, Š. Kos, A. Abanov, and D. Pines, *Phys. Rev. Lett.* **90**, 227202 (2003).
- [4] Y. Kawasaki, S. Kawasaki, M. Yashima, T. Mito, G.-q. Zheng, Y. Kitaoka, H. Shishido, R. Settai, Y. Haga, and Y. Ōnuki, *J. Phys. Soc. Jpn.* **72**, 2308 (2003).
- [5] M. Yashima, S. Kawasaki, Y. Kawasaki, G.-q. Zheng, Y. Kitaoka, H. Shishido, R. Settai, Y. Haga, and Y. Ōnuki, *J. Phys. Soc. Jpn.* **73**, 2073 (2004).
- [6] H. Sakai, S.-H. Baek, S. E. Brown, F. Ronning, E. D. Bauer, and J. D. Thompson, *Phys. Rev. B* **82**, 020501(R) (2010).
- [7] H. Sakai, S. E. Brown, S. H. Baek, F. Ronning, E. D. Bauer, and J. D. Thompson, *Phys. Rev. Lett.* **107**, 137001 (2011).
- [8] J. Paglione, M. A. Tanatar, D. G. Hawthorn, E. Boaknin, R. W. Hill, F. Ronning, M. Sutherland, L. Taillefer, C. Petrovic, and P. C. Canfield, *Phys. Rev. Lett.* **91**, 246405 (2003).
- [9] A. Bianchi, R. Movshovich, I. Vekhter, P. G. Pagliuso, and J. L. Sarrao, *Phys. Rev. Lett.* **91**, 257001 (2003).
- [10] F. Ronning, C. Capan, A. Bianchi, R. Movshovich, A. Lacerda, M. F. Hundley, J. D. Thompson, P. G. Pagliuso, and J. L. Sarrao, *Phys. Rev. B* **71**, 104528 (2005).
- [11] S. Singh, C. Capan, M. Nicklas, M. Rams, A. Gladun, H. Lee, J. F. DiTusa, Z. Fisk, F. Steglich, and S. Wirth, *Phys. Rev. Lett.* **98**, 057001 (2007).
- [12] S. Zaum, K. Grube, R. Schäfer, E. D. Bauer, J. D. Thompson, and H. v. Löhneysen, *Phys. Rev. Lett.* **106**, 087003 (2011).
- [13] Y. Tokiwa, E. D. Bauer, and P. Gegenwart, *Phys. Rev. Lett.* **111**, 107003 (2013).
- [14] L. D. Pham, T. Park, S. Maquilon, J. D. Thompson, and Z. Fisk, *Phys. Rev. Lett.* **97**, 056404 (2006).
- [15] M. Yokoyama, K. Fujimura, S. Ishikawa, M. Kimura, T. Hasegawa, I. Kawasaki, K. Tenya, Y. Kono, and T. Sakakibara, *J. Phys. Soc. Jpn.* **83**, 033706 (2014).
- [16] R. R. Urbano, B. L. Young, N. J. Curro, J. D. Thompson, L. D. Pham, and Z. Fisk, *Phys. Rev. Lett.* **99**, 146402 (2007).

- [17] H. Sakai, F. Ronning, J. X. Zhu, N. Wakeham, H. Yasuoka, Y. Tokunaga, S. Kambe, E. D. Bauer, and J. D. Thompson, *Phys. Rev. B* **92**, 121105(R) (2015).
- [18] H. Sakai, Y. Tokunaga, S. Kambe, J.-X. Zhu, F. Ronning, J. D. Thompson, S. K. Ramakrishna, A. P. Reyes, K. Suzuki, Y. Oshima, and M. Yokoyama, *Phys. Rev. B* **104**, 085106 (2021).
- [19] E. D. Bauer, F. Ronning, C. Capan, M. J. Graf, D. Vandervelde, H. Q. Yuan, M. B. Salamon, D. J. Mixson, N. O. Moreno, S. R. Brown, J. D. Thompson, R. Movshovich, M. F. Hundley, J. L. Sarrao, P. G. Pagliuso, and S. M. Kauzlarich, *Phys. Rev. B* **73**, 245109 (2006).
- [20] K. Gofryk, F. Ronning, J. X. Zhu, M. N. Ou, P. H. Tobash, S. S. Stoyko, X. Lu, A. Mar, T. Park, E. D. Bauer, J. D. Thompson, and Z. Fisk, *Phys. Rev. Lett.* **109**, 186402 (2012).
- [21] E. D. Bauer, N. O. Moreno, D. J. Mixson, J. L. Sarrao, J. D. Thompson, M. F. Hundley, R. Movshovich, and P. G. Pagliuso, *Phys. B: Condens. Matter* **359-361**, 35 (2005).
- [22] R. Otaka, M. Yokoyama, H. Mashiko, T. Hasegawa, Y. Shimizu, Y. Ikeda, K. Tenya, S. Nakamura, D. Ueta, H. Yoshizawa, and T. Sakakibara, *J. Phys. Soc. Jpn.* **85**, 094713 (2016).
- [23] E. D. Bauer, C. Capan, F. Ronning, R. Movshovich, J. D. Thompson, and J. L. Sarrao, *Phys. Rev. Lett.* **94**, 047001 (2005).
- [24] S. M. Ramos, M. B. Fontes, E. N. Hering, M. A. Continentino, E. Baggio-Saitovich, F. D. Neto, E. M. Bittar, P. G. Pagliuso, E. D. Bauer, J. L. Sarrao, and J. D. Thompson, *Phys. Rev. Lett.* **105**, 126401 (2010).
- [25] M. Yokoyama, K. Suzuki, K. Tenya, S. Nakamura, Y. Kono, S. Kittaka, and T. Sakakibara, *Phys. Rev. B* **99**, 054506 (2019).
- [26] P. Blaha, K. Schwarz, G. Madsen, D. Kvasnicka, and J. Luitz, WIEN2K, *An Augmented Plane Wave + Local Orbitals Program for Calculating Crystal Properties, Technical Report* (Technische Universität Wien, Vienna, Austria, 2001).
- [27] J. P. Perdew, K. Burke, and M. Ernzerhof, *Phys. Rev. Lett.* **77**, 3865 (1996).
- [28] J. Chepin, Jr., and J. J. H. Ross, *J. Phys.: Condens. Matter* **3**, 8103 (1991).
- [29] J. Ruzs, P. M. Oppeneer, N. J. Curro, R. R. Urbano, B.-L. Young, S. Lebègue, P. G. Pagliuso, L. D. Pham, E. D. Bauer, J. L. Sarrao, and Z. Fisk, *Phys. Rev. B* **77**, 245124 (2008).
- [30] T. Moriya, *J. Phys. Soc. Jpn.* **18**, 516 (1963).
- [31] T. Moriya and T. Takimoto, *J. Phys. Soc. Jpn.* **64**, 960 (1995).
- [32] N. J. Curro, B. Simovic, P. C. Hammel, P. G. Pagliuso, J. L. Sarrao, J. D. Thompson, and G. B. Martins, *Phys. Rev. B* **64**, 180514(R) (2001).
- [33] C. Stock, C. Broholm, J. Hudis, H. J. Kang, and C. Petrovic, *Phys. Rev. Lett.* **100**, 087001 (2008).
- [34] S. Raymond, K. Kaneko, A. Hiess, P. Steffens, and G. Lapertot, *Phys. Rev. Lett.* **109**, 237210 (2012).
- [35] C. Stock, C. Broholm, Y. Zhao, F. Demmel, H. J. Kang, K. C. Rule, and C. Petrovic, *Phys. Rev. Lett.* **109**, 167207 (2012).
- [36] S. Raymond and G. Lapertot, *Phys. Rev. Lett.* **115**, 037001 (2015).
- [37] C. Lacroix, A. Solontsov, and R. Ballou, *Phys. Rev. B* **54**, 15178 (1996).
- [38] G.-q. Zheng, H. Ozaki, W. G. Clark, Y. Kitaoka, P. Kuhns, A. P. Reyes, W. G. Moulton, T. Kondo, Y. Shimakawa, and Y. Kubo, *Phys. Rev. Lett.* **85**, 405 (2000).
- [39] Y. Kubo, T. Kondo, Y. Shimakawa, T. Manako, and H. Igarashi, *Phys. Rev. B* **45**, 5553 (1992).
- [40] S. Ikeda, H. Shishido, M. Nakashima, R. Settai, D. Aoki, Y. Haga, H. Harima, Y. Aoki, T. Namiki, H. Sato, and Y. Ōnuki, *J. Phys. Soc. Jpn.* **70**, 2248 (2001).
- [41] Y. Song, W. Wang, J. S. Van Dyke, N. Pouse, S. Ran, D. Yazici, A. Schneidewind, P. Čermák, Y. Qiu, M. B. Maple, D. K. Morr, and P. Dai, *Commun. Phys.* **3**, 98 (2020).
- [42] C. Stock, J. A. Rodriguez-Rivera, K. Schmalzl, F. Demmel, D. K. Singh, F. Ronning, J. D. Thompson, and E. D. Bauer, *Phys. Rev. Lett.* **121**, 037003 (2018).
- [43] Y. Kuramoto and K. Miyake, *J. Phys. Soc. Jpn.* **59**, 2831 (1990).
- [44] K. Miyake and O. Narikiyo, *J. Phys. Soc. Jpn.* **63**, 3821 (1994).
- [45] T. Moriya and K. Ueda, *Adv. Phys.* **49**, 555 (2000).
- [46] T. Moriya and K. Ueda, *Rep. Prog. Phys.* **66**, 1299 (2003).
- [47] S. Kambe, J. Flouquet, and T. E. Hargreaves, *J. Low Temp. Phys.* **108**, 383 (1997).
- [48] S. Kambe, J. Flouquet, P. Lejay, P. Haen, and A. de Visser, *J. Phys.: Condens. Matter* **9**, 4917 (1997).
- [49] K. Miyake and O. Narikiyo, *J. Phys. Soc. Jpn.* **63**, 2042 (1994).
- [50] R. Settai, H. Shishido, S. Ikeda, Y. Murakawa, M. Nakashima, D. Aoki, Y. Haga, H. Harima, and Y. Onuki, *J. Phys.: Condens. Matter* **13**, L627 (2001).
- [51] D. Hall, E. C. Palm, T. P. Murphy, S. W. Tozer, Z. Fisk, U. Alver, R. G. Goodrich, J. L. Sarrao, P. G. Pagliuso, and T. Ebihara, *Phys. Rev. B* **64**, 212508 (2001).
- [52] A. Koitzsch, I. Opahle, S. Elgazzar, S. V. Borisenko, J. Geck, V. B. Zabolotnyy, D. Inosov, H. Shiozawa, M. Richter, M. Knupfer, J. Fink, B. Büchner, E. D. Bauer, J. L. Sarrao, and R. Follath, *Phys. Rev. B* **79**, 075104 (2009).
- [53] A. Koitzsch, T. K. Kim, U. Treske, M. Knupfer, B. Büchner, M. Richter, I. Opahle, R. Follath, E. D. Bauer, and J. L. Sarrao, *Phys. Rev. B* **88**, 035124 (2013).